



HAL
open science

Modification of the optical properties and nano-crystallinity of anatase TiO₂ nanoparticles thin film using low pressure O₂ plasma treatment

Maria Mitronika, Jacopo Profili, Antoine Goulet, Luc Stafford, Agnès Granier, Mireille Richard-Plouet

► To cite this version:

Maria Mitronika, Jacopo Profili, Antoine Goulet, Luc Stafford, Agnès Granier, et al.. Modification of the optical properties and nano-crystallinity of anatase TiO₂ nanoparticles thin film using low pressure O₂ plasma treatment. *Thin Solid Films*, 2020, 709, pp.138212. 10.1016/j.tsf.2020.138212 . hal-03010324

HAL Id: hal-03010324

<https://hal.science/hal-03010324>

Submitted on 17 Dec 2020

HAL is a multi-disciplinary open access archive for the deposit and dissemination of scientific research documents, whether they are published or not. The documents may come from teaching and research institutions in France or abroad, or from public or private research centers.

L'archive ouverte pluridisciplinaire **HAL**, est destinée au dépôt et à la diffusion de documents scientifiques de niveau recherche, publiés ou non, émanant des établissements d'enseignement et de recherche français ou étrangers, des laboratoires publics ou privés.

Modification of the optical properties and nano-crystallinity of anatase TiO₂ nanoparticles thin film using low pressure O₂ plasma treatment

M. Mitronika¹, J. Profili², A. Gouillet¹, L. Stafford², A. Granier¹, M. Richard-Plouet¹

¹ Université de Nantes, CNRS, Institut des Matériaux Jean Rouxel, IMN, F-44000 Nantes, France

² Département de Physique, Université de Montréal, Montréal, Québec H2V 0B3, Canada

Abstract: TiO₂ nanoparticles (NPs) thin films with a thickness of 50 nm and a core-shell nanostructure were prepared using the spin coating technique and were treated using an inductively coupled O₂ plasma at low pressure. While no significant features were observed during pumping, two kinetics can be identified during plasma processing using *in situ* spectroscopic ellipsometry. For very short plasma treatment times, the removal of solvent-based organic moieties surrounding TiO₂ nanoparticles produces a densification of the inorganic TiO₂ films. Such mineralization effect by the O₂ plasma treatment was confirmed by X-ray photoelectron microscopy. For larger time scales, the average size of TiO₂ NPs rises and significant changes of the optical properties occur. While no significant changes in the film nanostructure were observed by Scanning Electron Microscopy, a rise in the crystallite size and an increase in the agglomeration of TiO₂ nanoparticles were confirmed by Transmission Electron Microscopy and Atomic Force Microscopy, respectively. The mechanisms involved in such plasma-induced modification of nanostructured TiO₂ thin films are discussed in line with the energy fluxes of plasma-generated species.

Keywords: Titanium dioxide; Nanoparticles, Thin films, Plasma-surface interactions, Plasma species energy fluxes

1. Introduction

Nanoparticles (NPs) have been widely investigated by the scientific community, as they give flexibility to a wide variety of applications, including photovoltaics [1], electrical insulation systems [2], electronic[3], photonic devices [4] and sensors[5]. The importance of NPs was especially realized when it was discovered that the size of the NPs can have an influence on the final properties compared to the bulk material. They can be classified depending on their nature (for example, carbon-based, ceramic,

metal, polymeric and semiconductor NPs[6]), size, morphology, physical and chemical characteristics, etc. Among the different systems, TiO₂, as high-k, stable and low cost semiconductor has been identified as an ideal candidate for its optical [7], dielectric[8-9] and photocatalytic[10] properties. Trying to expand these properties, TiO₂ NPs were extensively prepared and studied especially for cosmetic [11], antibacterial[12], solar cell[13–16], self-cleaning[17], hydrophobic [18] and isolative[19] applications. In addition, at the nanometre scale, especially below 10 nm, TiO₂ NPs can enlarge the bandgap and shift to larger redox potentials the band edges [20].

Today, the most common ways to deposit a layer of NPs dispersed in colloidal solution are dip casting, drop casting, spin coating and inkjet printing. While wet processes represent fast and low-cost deposition methods, they often result in poor-quality films due to the presence of solvent residues on the substrate. In an attempt to counterbalance this effect, a few studies have investigated the impact of weakly ionized, non-thermal plasma treatments on these wet-processed thin films of NPs. In particular, Homola et al. [21] have reported the mineralization effect of atmospheric pressure dielectric barrier discharge (~~DBD~~) on the inkjet-printed TiO₂ NPs film. In particular, they have indicated the possibility of acquiring high-quality inorganic TiO₂ films by removing the organic moieties of the binder. Chang et al. [22,23] have investigated the sintering effect of atmospheric pressure plasma jet (~~APPJ~~) on screen-printed TiO₂ NPs paste. Finally, there have been some reports aiming in the effective nitrogen doping of ordered, mesoporous TiO₂ thin films using nitrogen/argon (N₂/Ar) plasmas at low pressure [24].

In this framework, this study examines the treatment of thin films formed of spin-coated 5 nm anatase TiO₂ NPs [25] by an inductively coupled plasma operated in O₂ at low pressure. More precisely, through judicious control of the plasma properties and using both *ex situ* and *in situ* analysis of plasma-processed

thin films, we report on the influence of the plasma treatment time on the organic solvent, the TiO₂ crystallites and the nanostructuring of spin-coated TiO₂ NPs. In line with the experimental data and the energy fluxes of plasma-generated species at the substrate surface, the mechanisms involved in such plasma-induced modification are discussed.

2. Material and Methods

2.1 Spin-coating of TiO₂ nanoparticles

For wet deposition of TiO₂ thin films, a colloidal solution of crystallized anatase TiO₂ NPs was spin-coated on thermally oxidized silicon substrates (500 nm SiO₂ on 500 μm Si wafer). Before deposition, the SiO₂/Si substrates were cleaned in an ultrasonic bath with distilled water, ethanol and isopropanol. The colloidal solution, synthesized according to ref. [1] and [25], comprises TiO₂ NPs with a well-defined monodispersed mean hydrodynamic diameter centered at 5 nm. As synthesized, the solvent of this solution is a mixture of 4-methyl-1,3-dioxolan-2-one (also known as propylene carbonate (PC)) and 1,2-propanediol (or propylene glycol (PG)), with a molar fraction in PC, $x_{PC}=0.27$, where $x_{PC} = [PC]/([PC] + [PG])$. In order to deposit a highly-concentrated and sufficiently-thick layer of TiO₂ NPs by spin coating, the solution was concentrated by evaporating part of the solvent at 120 °C. Consequently, due to the lower volatility of PC with respect to PG, x_{PC} increases by enrichment in PC. As shown in Figure 1, such change in x_{PC} also modifies the viscosity of the solution (determined using a Lovis 2000 ME-Anton-Paar viscometer). In this work, $x_{PC}=0.6$ was used; thus upon further evaporation during spin coating, the viscosity remains in a narrow range of values [26].

Because achieving uniform films still remains a challenge by spin coating [27] and in order to get a homogeneous layer of TiO₂ NPs, a two-step spin coating program was chosen. More precisely, using Spin Processor Laurell WS-650Mz-23NPPB, the first step was set to a spinning speed of 1000 rpm for 30 seconds to ensure a homogeneous spread of the solution on the substrate surface. In the second step, a speed of 2000 rpm for 1 minute was used to activate the drying process of the spin-coated layer. After each spin-coating set, the substrate was dried at 150 °C for 10 minutes. To acquire a thickness of 40-50 nm, three spin-coating sets were performed.

2.2 Plasma Treatment of spin-coated TiO₂ nanoparticles

TiO₂ NPs spin-coated on SiO₂/Si substrates were exposed to a low-pressure inductively coupled O₂ plasma. All details on this plasma source can be found in previous publications [28–30]. Briefly, the plasma is sustained at 13.56 MHz using a helicon antenna and then expands into a stainless steel processing chamber where plasma-substrate interaction occurs. In this system, plasma gases are introduced at the top of the plasma source and the high-vacuum pumping system is located at the bottom of the processing chamber. The operating conditions (along with the corresponding plasma characteristics [7,28,29] recorded close to the substrate surface) used in this study are summarized in Table 1. SiO₂/TiO₂ thin films were positioned in the centre of the substrate holder located in the processing chamber. As detailed below, *in situ* spectroscopic ellipsometry (SE) measurements were recorded during pumping as well as during the 20 minutes plasma treatment (~~PT~~) in order to monitor any possible vacuum- and plasma-induced modification.

2.3 Thin film characterization

For the *in situ* monitoring of the effect of O₂ plasma during the treatment on the spin-coated thin film, a rotating compensator spectroscopic ellipsometer (J.A. Woollam M-2000) was mounted on the plasma system and aligned with the substrate surface. *In situ* SE measurements were conducted between 245 and 1000 nm at 71.7° incident angle.

The surface morphology of the films was monitored using Scanning Electron Microscopy (SEM) with JEOL JSM 7600F, in a secondary electron mode, operating at 5kV. Moreover, Atomic Force Microscopy (AFM) was used in tapping mode with AFM Nanowizard II (JPK Instruments) and an Al-coated cantilever (PPP-NCHR-50 from NANOSENSORS) with a free resonance frequency of 330 kHz and a typical spring constant of about 42 N/m, to investigate the nanostructured topography and roughness of the films. Using the ImageJ software, after adjustment of the image's threshold and transformation in a binary format, the size distribution of the NPs was deduced from the AFM scans. Direct Light Scattering (DLS) using Zetasizer NanoZS (Malvern) was used to analyze the size distribution of the NPs in the colloidal solution. High-resolution Transmission Electron Microscopy (TEM) with S/TEM Themis Z G3, operating at 300 keV, (Thermo Fisher Scientific) was used to examine the crystallinity of TiO₂ NPs and assess any evolution of their size.

X-ray Photoelectron Spectroscopy (XPS) on a Kratos Nova spectrometer with Al K α radiation at 1486.6 eV was used to investigate the chemical composition of the topmost surface. Neutralization of the surface was applied in order to avoid differential charging effect. Survey spectra were measured from 1200 to -2 eV (Binding Energy) using a pass energy of 160 eV while high-resolution spectra over specific

regions of interest were recorded with a pass energy of 40 eV. Short time measurements were undertaken (dwell of 100 per 0.1 eV step-scan for O1s, Ti 2p and 200 ms for C1s,). After checking that no X-ray damage was induced, the scans were summed up in order to increase the signal over noise ratio. The decomposition and fitting of the measured XPS peaks was carried out using CasaXPS software (Neal Fairley, Copyright© 2005 Casa Software Ltd, 2005). After accounting for the background using a U2-Tougaard background, Gaussian-Lorentzian (30-70 %) functions were selected to model the different components. Raman spectroscopy measurements were also performed using a microconfocal Raman microscope (Renishaw inVia). The instrument was equipped with a double edge filter to eliminate the Rayleigh scattering and a charged couple device (CCD) camera working at a temperature of 220 K with a 1024 by 256 pixel array. The setup was composed of a confocal microscope that was equipped with an automated XYZ table and an x50 magnification objective. The laser excitation source used was set at 514 nm and the focused power was checked to avoid any degradation of the samples. Therefore, the power was selected at 1.5 mW and a recording time of 1 s with an accumulation of 10 measurements was used.

3. Results

3.1 Kinetics driving the plasma-induced modification of nanostructured TiO₂ thin films

As mentioned above, *in situ* SE measurements were recorded during pumping as well as during the 20 minutes plasma treatment in order to monitor possible vacuum- and plasma-induced modification. Spectroscopic Ellipsometry is based on change in the polarization of incident light after reflection by the system under investigation, the ellipsometric ratio $\rho = \tan(\Psi)\exp(j\Delta)$ is typically analyzed from

the measured angles Psi and Delta. The corresponding evolution of Psi and Delta values with plasma treatment time at 633 nm wavelength is plotted in Figure 2.

Here, the measurement was initialized at the beginning of the reactor pumping. After about 97 minutes, the plasma was turned on (time 0 on the x-axis of figure 2) for 20 minutes and then SE measurements were stopped. While the Psi and Delta values remain stable during pumping, significant changes of both Psi and Delta can be seen during the first two minutes of the plasma treatment. During the 2nd to 10th minute, signal variation becomes less pronounced and a saturation is reached between 10 and 20 minutes.

Aiming at further understanding this kinetic evolution, especially in the first minutes of the plasma treatment, the *in situ* SE data recorded at each plasma treatment time were fitted using a model. The validity of this model, and therefore the evaluation of the accuracy of the fit, was estimated by the Mean Square Error (MSE) [31]. Initially, the ellipsometric model used for the before plasma treatment condition (time 0) was the one illustrated in Figure 3a. This model, typically used for plasma-deposited anatase TiO₂ thin films, is based on Tauc-Lorentz dispersion law with an optical energy gap (E_g) of 3.2 eV [32]. As seen in Figure 3a, this model reveals significant discrepancy (MSE=273) between the experimental (coloured) and simulated (dashed) lines. Therefore, a different model was required to adequately represent a film containing spin-coated anatase TiO₂ NPs. As mentioned in the experimental section, the colloidal solution with TiO₂ NPs contains PG and PC. In such conditions, Karpinsky et al. [25] have proposed a core shell configuration of these NPs. In detail, it was calculated that for 5 nm TiO₂ anatase NPs, a 4.7 Å hydroxylated and organic shell exists. In this framework, the TiO₂ nanostructured layer was modelled using Bruggeman Effective Medium Approximation (BEMA) with two materials: the TiO₂ anatase NPs expressed with the Tauc-Lorentz dispersion law [31] with an optical energy gap at

3.4 eV (due to the nanometre size of the TiO₂ [20,33]) and the low-density thin shell inducing separation between the nanoparticles and thus expressed as voids. As highlighted in Figure 3b, the BEMA model provides much better agreement between experimental and simulated values (MSE=11) and thus seems very well suited for the spin-coated TiO₂ NPs system, at least from the optical point of view. Similar very-good-quality fits were observed for all operating conditions (not shown here).

From the fit of Psi and Delta spectra recorded at each plasma treatment time, a variety of information such as the optical thickness of the film, the fraction of voids, the energy gap (E_g), the refractive index of the layer (n_{eff}) and the extinction coefficient (k_{eff}) can be extracted. Information on the optical roughness of the layer could also be analysed. However, due to the rather small thickness of the films examined in this work and their very small roughness, roughening effects in Psi and Delta analysis can only be estimated. Over the range of experimental conditions examined, optical roughness values deduced by spectroscopic ellipsometry were ~ round 2 nm. By fitting and extracting the spectral data as a function of treatment time, the plots given in Figure 4 were obtained. Focusing on the 20 first minutes of the plasma treatment, the time evolution of the film thickness, the fraction of voids and the energy gap (E_g) are displayed in Figure 4a while the optical constants as a function of wavelength for various plasma treatment times are presented in Figure 4b.

As a general trend, the film thickness, the fraction of voids and E_g decrease with plasma treatment time and then reach steady-state after 10 minutes of plasma treatment. However, further analysis reveals that two timeframes can be identified during the first 10 minutes. Between 0 and 2 minutes, the film thickness sharply decreases by almost 6 nm (14% of the total thickness) and the fraction of voids rapidly reaches 0. This means that the shells and the empty spaces separating TiO₂ NPs are removed: this brings

TiO₂ NPs closer together. Over this time frame, the energy gap remains more or less constant. On the other hand, between the 2nd and the 10th minute, the fraction of voids remains 0, the film thickness only slightly decreases and the energy gap (E_g) now decreases significantly. As reported elsewhere for TiO₂ systems [33,34], there is a clear dependence between the size of TiO₂ crystallites and the energy bandgap of the film. Therefore, the decrease in E_g , provided by spectroscopic ellipsometry between the 2nd and the 10th minute, suggests an increase in the crystallite size of the spin-coated TiO₂ crystallites during plasma treatment over this specific time frame.

Regarding the optical parameters of the nanostructured TiO₂ layer, Figure 4b reveals that the effective refractive index (n_{eff}) and the effective extinction coefficient (k_{eff}) both increase during plasma treatment, with a more prominent increase in the UV (240-340 nm) zone. In terms of spectroscopic ellipsometry, the observed plasma-induced modification during the first two minutes (fraction of voids becomes 0, reduction in the film thickness, NPs become closer) implies that the initial BEMA layer becomes an actual TiO₂ NPs layer. Then, the existing TiO₂ layer is further treated, resulting in an additional increase of the effective refractive index, as observed in Figure 4a. In the same manner, the shift in the onset of the extinction coefficient can be related to the decrease of E_g [35,36]. Nevertheless, both the refractive index and the extinction coefficient have lower values than the ones obtained for bulk, plasma-deposited TiO₂ films ($n = 2.3$ at 633 nm) due to the nanometric size of TiO₂ NPs in the nanostructured TiO₂ film obtained by spin coating [32].

3.3 Morphological and crystallinity analysis of the plasma-treated nanostructured TiO₂ thin films

Morphological analysis of nanostructured, spin-coated TiO₂ thin films were realized by SEM and AFM in order to better understand the optical changes observed in the previous section. Further investigations on the crystallinity of TiO₂ NPs were achieved by TEM. Typical SEM images, TEM images and AFM scans obtained before and after plasma treatment are shown in Figure 5. At the scale of SEM images (left-hand-side column in Figure 5), the film seems globally homogeneous even if some darker contrasts are detected. At this scale, we deduce that these features could be attributed to cracks allowing the solvent to be expelled during the spin-coating process. After the plasma treatment, the nanostructuration of the film globally remains intact. However, the number of the cracks seems slightly increased. Since the resolution of the SEM is at 10 nm, one can understand that the exact identification of the 5 nm NPs is impossible. From TEM images (also presented on the middle-right side column of Figure 5), the basal TiO₂ planes indicate crystallized TiO₂ NPs before and after plasma treatment. Before exposure to the low-pressure O₂ plasma, typical crystallite sizes can be estimated at 3.5 ± 0.6 nm whereas after the plasma treatment the typical crystallite sizes increases to 4.5 ± 0.9 nm.

AFM was used as a local probe first to have access to the roughness and second to the size distribution of the NPs. As shown in figure 5 (middle-left column), the root-mean-square (RMS, Rq) roughness of as-deposited and plasma-treated TiO₂ films is 2.6 nm. These values are consistent with those estimated from spectroscopic ellipsometry (Section 3.1). Before the plasma treatment, Figure 5a reveals that AFM scans at low magnification are kind of fuzzy and blurry. Such feature can most likely be ascribed to the presence of solvent expelled throughout the film thickness that remains on the film surface after spin-coating of the colloidal solution. In contrary, after the plasma treatment, the quality of the image is significantly improved such that the shape and size of TiO₂ NPs can now readily be identified from both low and high magnification images. Cross sectional line profile from the same AFM scans are given in

Figure 5 (right-hand-side column). Despite the fact that these two profiles have the same R_q (RMS) roughness, which is extracted from the total area of the scan, they reveal some differences. From the as-deposited film, the height variation is more pronounced. Contrary, after the plasma treatment, the height variation is smoothed and the variation is less frequent. From these two particular profiles, the peak-to-valley R_t reaches 14.6 and 11.4 nm, before and after plasma treatment, respectively. This indicates that the surface of the NPs is affected by the treatment.

From detailed analysis of multiple AFM scans at low and high magnification, the mean size of spin-coated TiO_2 NPs before and after plasma treatment were extracted. The results are plotted as histograms in Figure 6. Size distribution obtained from DLS in the colloidal solution is also shown for comparison. From the plots, Gaussian fits were realized to obtain the mean size and the standard deviation. Compared to the DLS results of TiO_2 NPs in volume, the hydrodynamic diameter increases after the spin-coating process. In the colloidal solution, the hydrodynamic diameter is estimated at 4.0 nm and the standard deviation is at 0.3 nm. After the spin-coating process, these values increase to 13 nm and 4 nm, respectively. Such feature was also observed by other authors (see, for example, [37,38]) and was ascribed to the agglomeration of TiO_2 NPs during deposition and evaporation of the solvent. Therefore, the objects observed and measured by AFM are aggregated TiO_2 NPs. After the plasma treatment, there is a slight shift of these aggregations to higher values, with a mean size of 16 nm and a standard deviation of 5 nm. The fact that the mean size increases with a relatively low standard deviation in AFM scans is consistent with previous observations that there is a shift towards higher NPs sizes of TiO_2 NPs after plasma treatment, observed from SE (section 3.1) associated to an increase in crystallite size as stated from High Resolution TEM observations (Middle of Figure 5).

3.3 Chemical analysis of the plasma-treated nanostructured TiO₂ thin films

For the chemical analysis of the spin-coated TiO₂ NPs before and after the plasma treatment, Raman spectroscopy and XPS were used. Figure 7 presents the Raman spectra of TiO₂ NPs before and after plasma treatment with a focus on the Eg band anatase peak. Raman modes can be assigned to the Raman spectra of the anatase crystal: 147 (Eg), 200 (Eg), 400 (B1g), 513 (A1g), 518 (B1g) and 642 cm⁻¹ (Eg) [39,40]. Since commenting Raman intensities of very thin films requires to be cautions, the analysis was limited to the peak positions. Regarding the spin-coated films before plasma treatment, it can be observed that the Eg peak lies at 154 cm⁻¹: this value is shifted from the expected anatase 144 cm⁻¹ Eg peak [41,42]. It is well-established experimentally that Raman spectra of low-dimensional crystals of semiconductors are modified when compared to the corresponding bulk crystal spectra namely, (1) the Raman peaks are asymmetrically broadened and (2) their positions are shifted [43,44]. In this context, the results presented in Figure 7 confirm that spin-coated TiO₂ NPs are anatase crystallites and small in size. Moreover, after the plasma treatment, the Eg band peak maintains a similar asymmetrical shape but shifts to 150 cm⁻¹; such feature can be related to an increase in the mean crystallite size of TiO₂ NPs [42,45], in very good agreement with the conclusions of *in situ* spectroscopic ellipsometry (Section 3.1) and TEM (middle of Figure 5) in Section 3.3.

Further chemical analysis was obtained through XPS. As reported by many authors (see, for example, [1,46,47]), the signal of titanium element in XPS results from two separated peaks that can be attributed to Ti 2p_{3/2} and Ti 2p_{1/2}. The 2p_{3/2} peak lies at 458.5 eV as expected for Ti⁴⁺ cations in TiO₂. The contribution of oxygen bonded to titanium atoms and noted as Ti-O appears at 530.0eV. Since the colloidal solution of TiO₂ NPs was synthesized in an organic solvent, the contribution of carbon element

was considered. Therefore, three peaks were identified. The first, at 284.8eV, is usually assigned to C-C bonds of both adventitious elemental carbon and the solvent, while the second, at 286.0eV, and the third, 288.5eV, can be related to -C-O bonds and C=O bonds, respectively. Fitting these peaks with CasaXPS software can then provide information on the atomic percentage of the various contributions in nanostructured TiO₂ films. The results are presented in Figure 8 before and after plasma treatment. As expected, the pristine surface reveals a rather significant amount of organic species (40% in total). After the O₂ plasma treatment, this contribution significantly decreases (22% in total) due to the removal of solvent-based organic moieties.

4. Discussion

Based on the experimental data presented in Section 3, the main effects observed after the O₂ plasma treatment of the spin-coated TiO₂ nanostructured thin film are (i) a mineralization of the film due to the removal of solvent-based organic moieties surrounding TiO₂ NPs (evidenced by XPS and AFM), (ii) a densification of the film (evidenced by *in situ* SE) and (iii) an increase of the crystallite size and of the agglomeration of TiO₂ NPs (evidenced by *in situ* SE, AFM, TEM, and Raman spectroscopy). A way to explain these features is by understanding both the nanoparticles and the O₂ plasma itself. On the one hand, as already mentioned, Karpinsky et al. [25] have proposed a core shell configuration for TiO₂ NPs synthesised according to ref. [1] and [25]. As a result, for the case of 5 nm TiO₂ anatase NPs dispersed in PC and PG, a 4.7 Å hydroxylated and organic shell exists around TiO₂ NPs. On the other hand, over the range of experimental conditions investigated (see all details in Table 1, [29]), the population of O atoms ($n_o=1.7 \times 10^{14} \text{ cm}^{-3}$) is much larger than the O₂⁺ ion density ($n_i=1.6 \times 10^9 \text{ cm}^{-3}$). This predominance of O atoms in the low-pressure plasma promotes their interaction with the film and thus provides a

smooth and selective chemical etching rather than rapid and non-selective ion bombardment. Based on these features, an attempt to illustrate the effect of the O₂ plasma treatment on TiO₂ NPs is presented in Figure 9.

During the first kinetics characterized by a fairly constant energy gap (and thus crystallite size) and a significant decrease of the film thickness and of the fraction of voids (0-2min, see Figure 4), chemical etching of the organic part of the NPs' shell occurs, densifying the layer and leading to the production of CO, CO₂ and H₂O volatile by-products in the plasma volume [29]. This behavior, depicted in Figure 9b, can be confirmed by the decrease of the concentration fraction of organic species measured by XPS. During the second kinetics characterized by a decrease of the energy gap (and thus a rise of the crystallite size) and of the film thickness (2-10min, see Figure 4), the O atoms have better access to the total thickness of the film such that they become able to reorganize the remaining shell with the core. This reorganization leads to an even thinner shell and to the addition of a TiO₂ layer surrounding the initial TiO₂ core by the formation of O-Ti-O bonds. These aspects are illustrated in Figures 9c and 9d and ultimately lead to the configuration displayed in Figure 9e. Through both *in situ* SE and Raman spectroscopy, it can be verified that this layer is contributing to the growth of the total TiO₂ crystallites, meaning that they remain in an anatase and not amorphous phase.

Many groups have attempted to investigate the mechanism leading to the crystallization of amorphous NPs in weakly ionized, non thermal plasmas [48–50]. The plasma-particle interactions leading to the heating of the TiO₂ NPs could be a suitable explanation to this phase transformation in O₂ plasmas at low pressure. In order to estimate the temperature of the NPs (T_{NPs}) over the range of experimental conditions examined, a steady-state power balance equation $Q_{IN} = Q_{OUT}$ was used [48,49]. In this case, the simple model of a single NP on the substrate surface was used. Here, the total input power Q_{IN} and

total output power Q_{OUT} at the NPs' surface can be obtained from the corresponding energy fluxes J_{IN} and J_{OUT} , $Q_{IN} = \int_A J_{IN} dA = \int_A J_{OUT} dA$, where the integrals are performed over the studied surface area.

During the O₂ plasma treatment, the total input energy flux includes the contributions of positive ions (J_{ions}) following either their acceleration in the plasma sheath surrounding the NP at floating potential or their neutralization at the NP surface. In addition, electrons (J_e) as a result of their random motion around the NP at floating potential and O atoms (J_{ass}) following their recombination-association event at the NP surface. In this framework, the total energy flux towards the NPs can be written as [48,49]:

$$J_{IN} = J_{ions} + J_e + J_{ass} = n_i \sqrt{\frac{k_B T_e}{m_i}} (E_{ion} + \Gamma_i E_i) + n_i \sqrt{\frac{k_B T_e}{m_i}} 2k_B T_e + \frac{1}{4} n_O \sqrt{\frac{8k_B T_g}{\pi m_O}} \Gamma_O E_{diss} \quad (1)$$

where k_B is the Boltzmann constant, m_i is the mass of O₂⁺, $E_{ion} = e (V_p - V_f)$ is the sheath potential (where V_p is the plasma potential, V_f is the floating potential and e is the electron charge), Γ_i is the recombination coefficient of the positive ions on the NP surface (here, $\Gamma_i = 1$ is assumed), E_i is the ionization energy (12.06 eV for O₂), m_O is the mass of O atoms, E_{diss} is the dissociation energy (5 eV for O₂), and Γ_O is the recombination coefficient of O atoms on the TiO₂ NP surface. Over the range of experimental conditions investigated, the Γ_O value can be estimated between 0.4 and 1 [51] (here, a maximum contribution was assumed such that $\Gamma_O = 1$). For the 3.3 Pa, O₂ plasma investigated in this

study, all of these contributions can be calculated using the plasma characteristics ($n_i, n_e, n_0, E_{ion}, T_e, T_g, T_s$) listed in Table 1. As shown in Table 2, the main contribution to the total input energy flux is J_{ass} .

Regarding the total output energy flux J_{OUT} (heat loss term), the contributions include thermal conduction with the neutral gas species striking onto the NP surface ($J_{cond,gas}$), thermal conduction with atoms from the solid substrate ($J_{cond,solid}$) and radiation cooling (J_{rad}). For the 3.3 Pa, O₂ plasma, the mean free path of the gas molecules (λ_{gas}) is much higher than the diameter of TiO₂ NPs such that the equation used for thermal conduction effects is the one for the free-molecule regime [52]. In this context, J_{OUT} can be written as follows [53]:

$$J_{OUT} = J_{cond,gas} + J_{cond,solid} + J_{rad} = \frac{\gamma+1}{16(\gamma-1)} \alpha \frac{p}{\sqrt{T_g}} \sqrt{\frac{8k_B}{\pi m}} (T_{NPS} - T_g) + \frac{\lambda_s}{d_s} (T_{NPS} - T_s) + \epsilon \sigma (T_{NPS}^4 - T_g^4) \quad (2)$$

where γ is the adiabatic coefficient ($\gamma=1.4$ for oxygen), α is the accommodation coefficient ($\alpha=0.9$ for oxygen), p is the pressure, m is the mass of gas molecules, ϵ is the emissivity of the TiO₂ NPs, and σ is the Stefan-Boltzmann constant. For the heat loss by thermal conduction with the solid, d_s is the thickness of the substrate ($d_s=500 \mu\text{m}$ for SiO₂/Si substrate) and λ_s is the heat conductivity of Si which is the main material of the substrate ($\lambda_s=130 \text{ Wm}^{-1}\text{K}^{-1}$). In the last term of Equation (2), the emissivity is $\epsilon=0.8$ [54]. For the 3.3 Pa, O₂ plasma examined in this study, the main contribution to the total output energy flux J_{OUT} comes from $J_{cond,solid}$ and from $J_{cond,gas}$. In this context, assuming $Q_{IN} = Q_{OUT}$ Equations (1) and (2) can be simplified as

$$Q_{IN} = A_p \frac{1}{4} n_O \sqrt{\frac{8k_B T_g}{\pi m_O}} E_{diss} = A_{cont} \frac{\lambda_s}{d_s} (T_{NPS} - T_s) + A_p \frac{\gamma+1}{16(\gamma-1)} \alpha \frac{p}{\sqrt{T_g}} \sqrt{\frac{8k_B}{\pi m}} (T_{NPS} - T_g) = Q_{OUT}$$

(3)

were A_p is the surface integral of the NP area i.e. $A_p = 4\pi r_p^2$, with a NPs's radius $r_p=2.5$ nm for the case of 5 nm TiO₂ anatase NPs and A_{cont} the cross-sectional area between the NP and the plane substrate.

Assuming a round sphere in contact with a plane, based on Hertz equation, $a = \sqrt[3]{\frac{3Wr_p}{4E^*}}$ [55], the radius of the spherical cap in contact can be deduced. W is the weight of the NP, r_p its radius and E^* is the effective elasticity modulus between the TiO₂ NP and the SiO₂/Si substrate. The resulting radius is significantly low verifying the assumption that the contact between the NP and the substrate is a single point.

For a typical substrate temperature of $T_s=400$ K (as measured by temperature-sensitive labels located at the substrate's backside [7]), the temperature of the NPs can be estimated to $T_{NPS}=744$ K. This value indicates that the conduction of the substrate is negligible due to the geometry (small contact area) of the system under consideration, the main cooling parameter is the one of the conduction with the gas and T_{NPS} becomes comparable to the temperature achieved for NPs in the gas phase of dusty plasmas [48,49,56]. Crystallization of amorphous TiO₂ NPs or nanotubes (NT) has been studied by several authors using either thermal annealing (furnaces) or hydrothermal treatment techniques. In such conditions, crystallization temperatures in the 720 - 1070 K and 320-470 K ranges have been reported for thermal annealing and hydrothermal treatments, respectively [25,57–60]. Ohsaki et al. [61] have also investigated the transformation of sol-gel derived TiO₂ films by RF plasma at a substrate temperature

lower than 400 K and a duration of treatment at 2 min. From these studies, it seems that the energy fluxes of plasma-generated species, and thus the corresponding values of T_{NPs} (especially on the topmost surface), obtained over the range of plasma conditions investigated are sufficient to induce a transformation of the additional TiO₂ thin amorphous layer to form anatase TiO₂ NPs with larger crystallite sizes than in as-deposited, spin-coated TiO₂ thin films.

5. Conclusion

Through this study, we have investigated the impact of a low pressure O₂ plasma on thin films formed of spin-coated anatase TiO₂ nanoparticles with a core shell configuration. It was shown that the pumping process for acquiring a low-pressure environment in the plasma reactor does not affect the optical properties of the films measured by in situ spectroscopic ellipsometry. In contrast, two kinetics were identified during plasma processing. For very short plasma treatment times, chemical etching of the hydroxyl and organic shell by O atoms induces a mineralization of the nanostructured TiO₂ film with no significant changes in the film morphology and nano-crystallinity. For larger time scales, a rise in the crystallite size of anatase TiO₂ NPs was first suggested from in situ spectroscopic ellipsometry and then confirmed by TEM and Raman analysis. In line with this finding, a rise of the size of TiO₂ agglomerates was also observed by AFM. In addition, a significant increase of the effective refractive index and extinction coefficient was highlighted. Based on this complete set of data, it was proposed that following chemical etching of the hydroxyl and organic shell, the O₂ plasma treatment can produce an additional TiO₂ layer surrounding the initial TiO₂ core through the formation of O-Ti-O bonds. In addition, given the relatively high temperature of TiO₂ nanoparticles provided by the energy balance between input energy fluxes (mostly through heterogeneous recombination of O atoms on the nanoparticles surface)

and output energy fluxes (mostly through thermal conduction with atoms from the surrounding gas), it was concluded that they remain in an anatase and not amorphous phase. Overall, low-pressure O₂ plasma treatments represent fast and efficient post-deposition tools for tailoring, with a degree of control, the optical properties and nano-crystallinity of the TiO₂ thin films formed of spin-coated anatase TiO₂ nanoparticles. Based on these results, we infer that tuning the plasma parameters (change the plasma species) could possibly give additional degrees of freedom to clean and heal the surface of oxide NPs, especially in case they are prepared in solution. Thus demonstrating that the NPs surface can be made accessible for reactive species by plasma treatment for short duration, is of great interest in the many fields such as electrochemistry or photocatalysis.

Acknowledgements

The authors would like to thank N. Gautier and N. Stephant for their technical support in TEM and SEM sessions. The authors would also like to thank the International Research Network on Nanomatériaux Multifonctionnels Contrôlés (IRN-NMC) for the financial support of the French-Canadian collaboration.

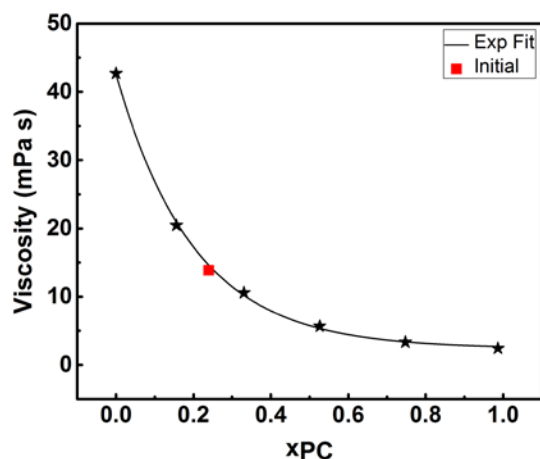


Figure 1: Graph of viscosity to the molar fraction in propylene carbonate x_{pc} value. The values indicated by black stars are experimental ones using reference solutions with different starting x_{pc} values; the red square corresponds to as-synthesized colloidal solution.

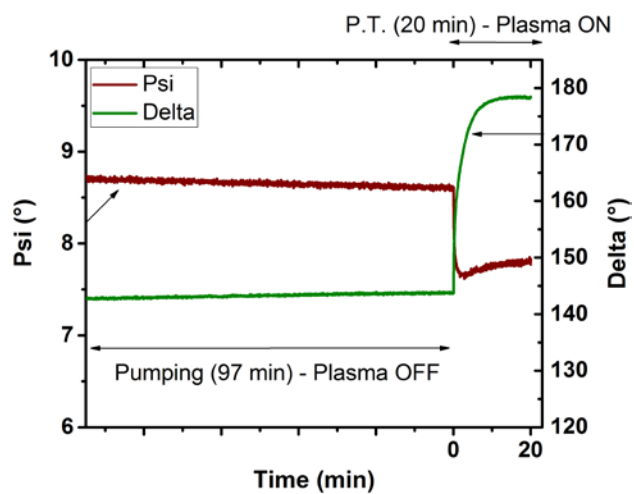


Figure 2: *In situ* evolution of Psi and Delta values with time, during the pumping and the 20-minutes plasma treatment. Results are shown for only one sample although comparable values were observed for other samples.

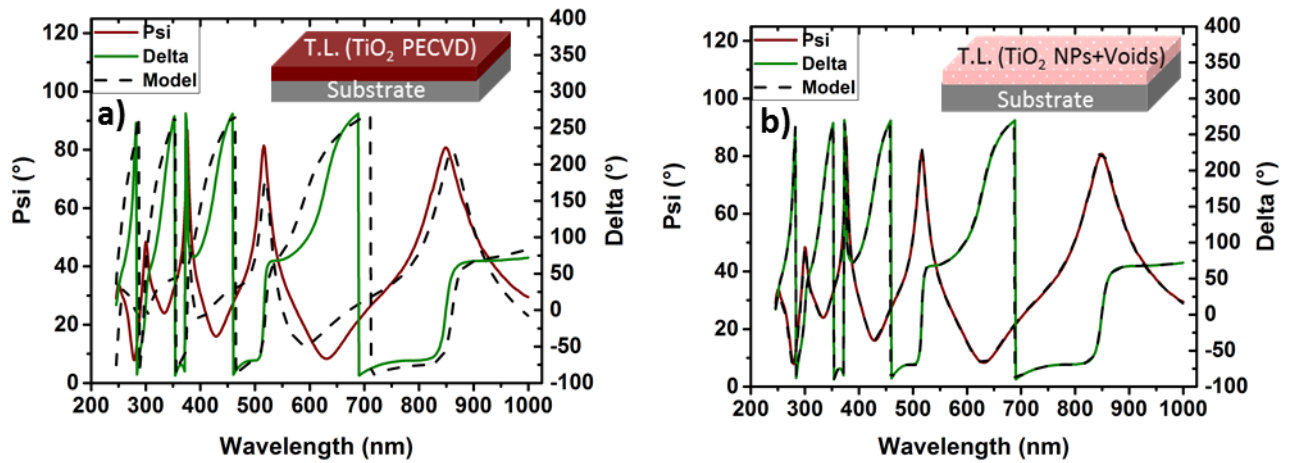


Figure 3: Psi-Delta values obtained from *in situ* spectroscopic ellipsometry before plasma treatment (full lines) and from simulations (dashed lines). The results are shown as a function of the photon wavelength. In a), the model is based on a plasma-deposited anatase TiO₂ material (TL, for Tauc-Lorentz dispersion law) whereas in b) the model relies on a combination of TiO₂ NPs and void (BEMA, for Bruggeman Effective Medium Approximation). The schematic representation of the models are also shown in the topmost figures.

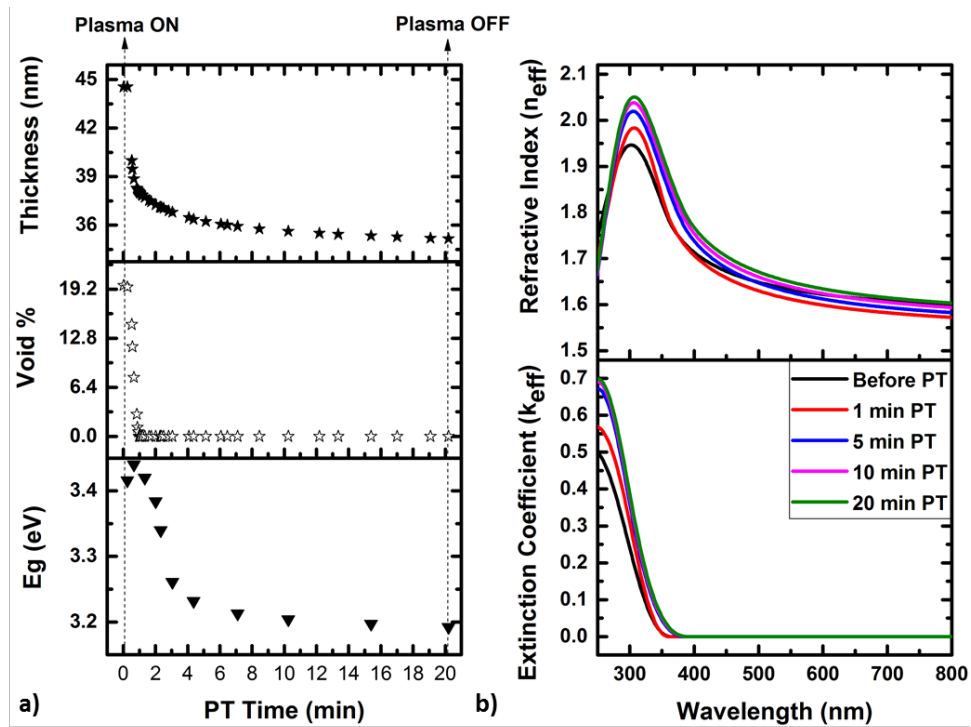


Figure 4: a) *In situ* spectroscopic ellipsometry results indicating the thickness evolution, the percentage of void, and the energy gap during the 20 minutes of the plasma treatment. b) Evolution of the effective refractive index (n_{eff}) and effective extinction coefficient (k_{eff}) for different times during the 20 minutes plasma treatment (PT). Black, red, blue, purple and green lines correspond to Before PT., 1 min, 5 min, and 10 min.

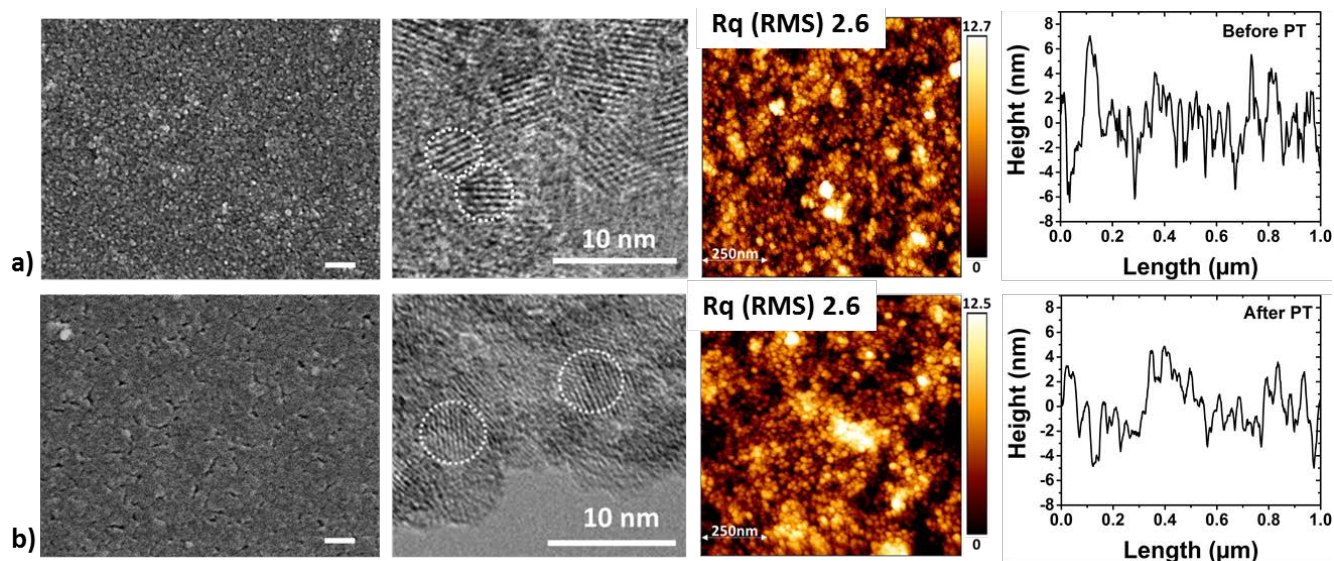


Figure 5: (from the left) Surface Scanning Electron Microscopy (SEM) Images, Transmission Electron Microscopy images, Atomic Force Microscopy (AFM) scans and cross sectional line profiles AFM of the a) non treated spin coated TiO₂ nanoparticles (NPs) thin film and b) 20 minutes plasma treated TiO₂ NPs thin film. Scale bar for SEM: 100 nm and Root Mean Square (RMS) Rq roughness values are indicated on the AFM scans.

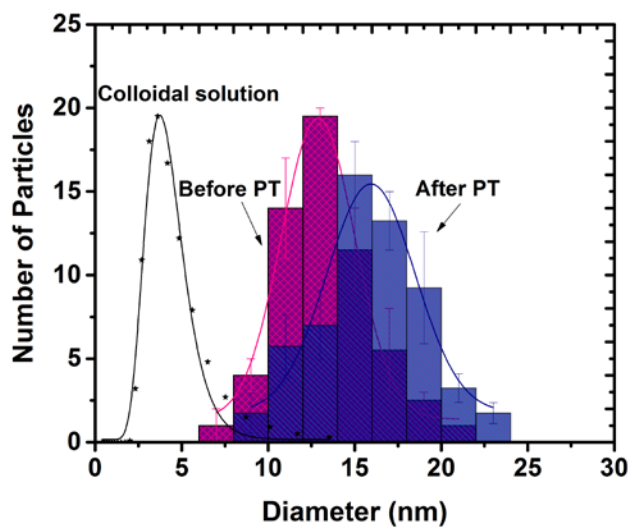


Figure 6: Size distribution of TiO₂ nanoparticles (NPs) deduced from Atomic Force Microscopy scans before (magenta) and after (blue) plasma treatment for 20 minutes. The size distribution of TiO₂ NPs obtained from Dynamic Light Scattering in the colloidal solution (black) before spin coating is also shown for comparison.

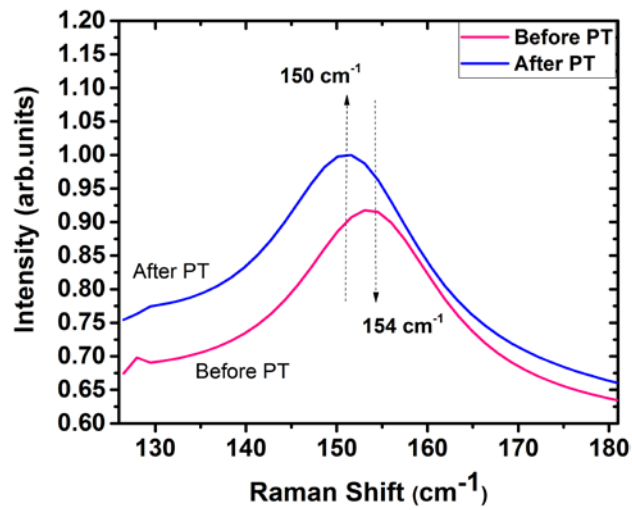


Figure 7: Anatase Eg Raman band before (pink) and after plasma treatment (blue).

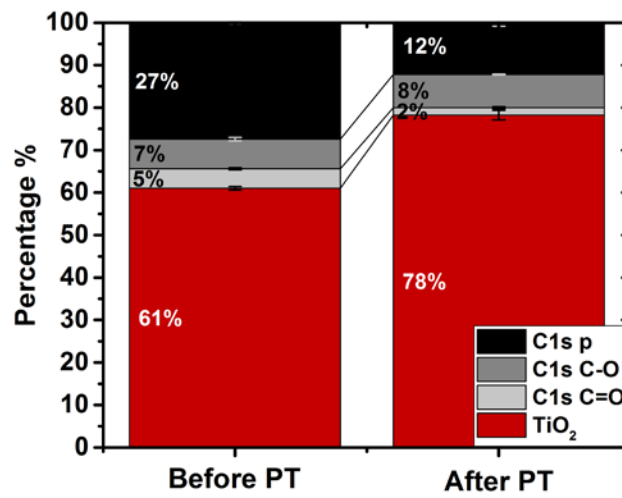


Figure 8: Stacked columns (%) of the chemical composition of the TiO₂ thin film surface before and after the plasma treatment.

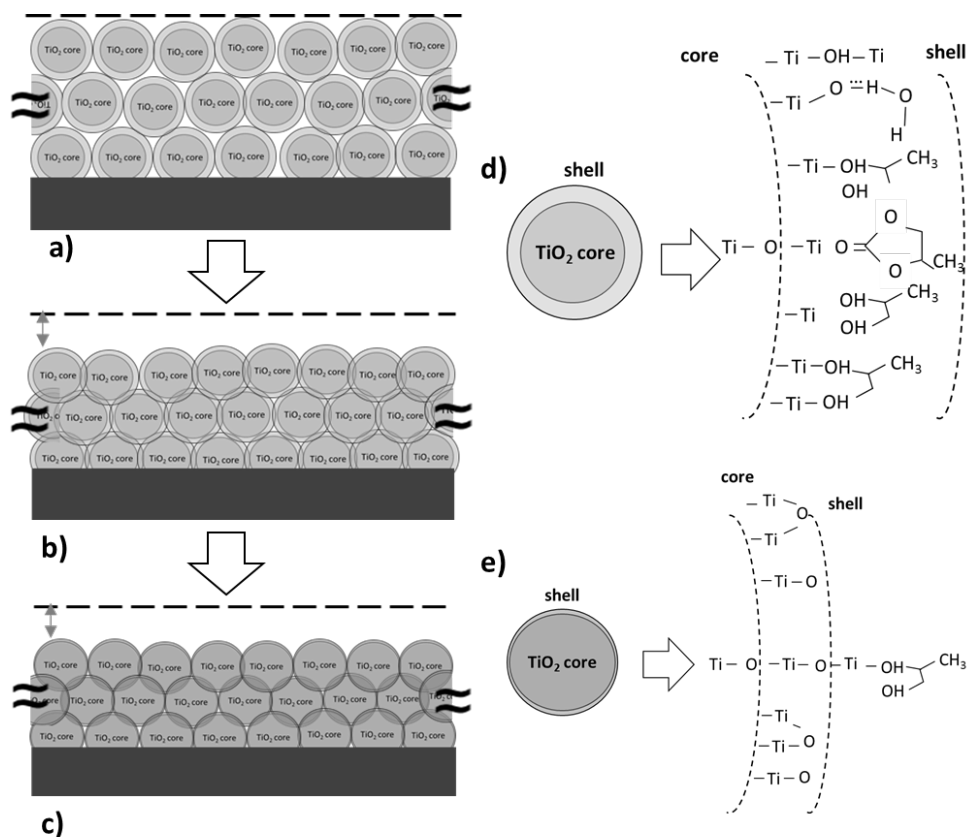


Figure 9: Schematic illustration of the spin-coated TiO₂ nanoparticles (NPs) a) before the plasma treatment, b) during the first kinetics (1-2 min) and c) during the second kinetics (3-15 min). Schematic illustration of the d) as synthesized, TiO₂ NPs, in core-shell configuration and e) after the plasma treatment.

References

- [1] M. El Kass, L. Brohan, N. Gautier, S. Béchu, C. David, N. Lemaitre, S. Berson, M. Richard-Plouet, TiO₂ Anatase Solutions for Electron Transporting Layers in Organic Photovoltaic Cells, *ChemPhysChem*. 18 (2017) 2390–2396. <https://doi.org/10.1002/cphc.201700306>.
- [2] J.K. Nelson, ed., *Dielectric polymer nanocomposites*, Springer, New York, 2010.

- [3] S. Sun, Monodisperse FePt Nanoparticles and Ferromagnetic FePt Nanocrystal Superlattices, *Science*. 287 (2000) 1989–1992. <https://doi.org/10.1126/science.287.5460.1989>.
- [4] J.D.B. Bradley, C.C. Evans, J.T. Choy, O. Reshef, P.B. Deotare, F. Parsy, K.C. Phillips, M. Lončar, E. Mazur, Submicrometer-wide amorphous and polycrystalline anatase TiO₂ waveguides for microphotonic devices, *Opt. Express*. 20 (2012) 23821. <https://doi.org/10.1364/OE.20.023821>.
- [5] T. Bora, Recent Developments on Metal Nanoparticles for SERS Applications, in: M.S. Seehra, A.D. Bristow (Eds.), *Noble Precious Met. - Prop. Nanoscale Eff. Appl.*, InTech, 2018. <https://doi.org/10.5772/intechopen.71573>.
- [6] I. Khan, K. Saeed, I. Khan, Nanoparticles: Properties, applications and toxicities, *Arab. J. Chem.* 12 (2017) 908–931. <https://doi.org/10.1016/j.arabjc.2017.05.011>.
- [7] D. Li, M. Carette, A. Granier, J.P. Landesman, A. Goulet, Effect of ion bombardment on the structural and optical properties of TiO₂ thin films deposited from oxygen/titanium tetraisopropoxide inductively coupled plasma, *Thin Solid Films*. 589 (2015) 783–791. <https://doi.org/10.1016/j.tsf.2015.07.015>.
- [8] D.K. Sarkar, D. Brassard, M.A.E. Khakani, L. Ouellet, Dielectric properties of sol–gel derived high-k titanium silicate thin films, *Thin Solid Films*. 515 (2007) 4788–4793. <https://doi.org/10.1016/j.tsf.2006.11.155>.
- [9] D. Brassard, D.K. Sarkar, M.A. El Khakani, L. Ouellet, Compositional effect on the dielectric properties of high-k titanium silicate thin films deposited by means of a cosputtering process, *J. Vac. Sci. Technol. Vac. Surf. Films*. 24 (2006) 600–605. <https://doi.org/10.1116/1.2180267>.

- [10] D. Li, S. Bulou, N. Gautier, S. Elisabeth, A. Goullet, M. Richard-Plouet, P. Choquet, A. Granier, Nanostructure and photocatalytic properties of TiO₂ films deposited at low temperature by pulsed PECVD, *Appl. Surf. Sci.* 466 (2019) 63–69. <https://doi.org/10.1016/j.apsusc.2018.09.230>.
- [11] M. Auffan, M. Pedeutour, J. Rose, A. Masion, F. Ziarelli, D. Borschneck, C. Chaneac, C. Botta, P. Chaurand, J. Labille, J.-Y. Bottero, Structural Degradation at the Surface of a TiO₂-Based Nanomaterial Used in Cosmetics, *Environ. Sci. Technol.* 44 (2010) 2689–2694. <https://doi.org/10.1021/es903757q>.
- [12] K. Jamuna-Thevi, S.A. Bakar, S. Ibrahim, N. Shahab, M.R.M. Toff, Quantification of silver ion release, in vitro cytotoxicity and antibacterial properties of nanostructured Ag doped TiO₂ coatings on stainless steel deposited by RF magnetron sputtering, *Vacuum.* 86 (2011) 235–241. <https://doi.org/10.1016/j.vacuum.2011.06.011>.
- [13] T. Homola, M. Shekargoftar, P. Dzik, R. Krumpolec, Z. Ďurašová, M. Veselý, M. Černák, Low-temperature (70 °C) ambient air plasma-fabrication of inkjet-printed mesoporous TiO₂ flexible photoanodes, *Flex. Print. Electron.* 2 (2017) 035010. <https://doi.org/10.1088/2058-8585/aa88e6>.
- [14] B. O'Regan, M. Grätzel, A low-cost, high-efficiency solar cell based on dye-sensitized colloidal TiO₂ films, *Nature.* 353 (1991) 737–740. <https://doi.org/10.1038/353737a0>.
- [15] D. Adak, S. Ghosh, P. Chakrabarty, A. Mondal, H. Saha, R. Mukherjee, R. Bhattacharyya, Self-cleaning V-TiO₂:SiO₂ thin-film coatings with enhanced transmission for solar glass cover and related applications, *Sol. Energy.* 155 (2017) 410–418. <https://doi.org/10.1016/j.solener.2017.06.014>.

- [16] D. Adak, S. Ghosh, P. Chakraborty, K.M.K. Srivatsa, A. Mondal, H. Saha, R. Mukherjee, R. Bhattacharyya, Non lithographic block copolymer directed self-assembled and plasma treated self-cleaning transparent coating for photovoltaic modules and other solar energy devices, *Sol. Energy Mater. Sol. Cells*. 188 (2018) 127–139. <https://doi.org/10.1016/j.solmat.2018.08.011>.
- [17] S. Guldin, P. Kohn, M. Stefik, J. Song, G. Divitini, F. Ecarla, C. Ducati, U. Wiesner, U. Steiner, Self-Cleaning Antireflective Optical Coatings, *Nano Lett.* 13 (2013) 5329–5335. <https://doi.org/10.1021/nl402832u>.
- [18] H. Bellanger, T. Darmanin, E. Taffin de Givenchy, F. Guittard, Chemical and Physical Pathways for the Preparation of Superoleophobic Surfaces and Related Wetting Theories, *Chem. Rev.* 114 (2014) 2694–2716. <https://doi.org/10.1021/cr400169m>.
- [19] Y. Du, Y. Lv, F. Wang, X. Li, C. Li, Effect of TiO₂ nanoparticles on the breakdown strength of transformer oil, in: 2010 IEEE Int. Symp. Electr. Insul., IEEE, San Diego, CA, USA, 2010: pp. 1–3. <https://doi.org/10.1109/ELINSL.2010.5549772>.
- [20] S.M. Gupta, M. Tripathi, A review of TiO₂ nanoparticles, *Chin. Sci. Bull.* 56 (2011) 1639–1657. <https://doi.org/10.1007/s11434-011-4476-1>.
- [21] T. Homola, P. Dzik, M. Veselý, J. Kelar, M. Černák, M. Weiter, Fast and Low-Temperature (70 °C) Mineralization of Inkjet Printed Mesoporous TiO₂ Photoanodes Using Ambient Air Plasma, *ACS Appl. Mater. Interfaces*. 8 (2016) 33562–33571. <https://doi.org/10.1021/acsami.6b09556>.
- [22] H. Chang, Y.-J. Yang, H.-C. Li, C.-C. Hsu, I.-C. Cheng, J.-Z. Chen, Preparation of nanoporous TiO₂ films for DSSC application by a rapid atmospheric pressure plasma jet sintering process, *J. Power Sources*. 234 (2013) 16–22. <https://doi.org/10.1016/j.jpowsour.2013.01.113>.

- [23] H. Chang, C.-M. Hsu, P.-K. Kao, Y.-J. Yang, C.-C. Hsu, I.-Chun. Cheng, J.-Z. Chen, Dye-sensitized solar cells with nanoporous TiO₂ photoanodes sintered by N₂ and air atmospheric pressure plasma jets with/without air-quenching, *J. Power Sources*. 251 (2014) 215–221. <https://doi.org/10.1016/j.jpowsour.2013.11.051>.
- [24] S.Z. Islam, A. Reed, D.Y. Kim, S.E. Rankin, N₂/Ar plasma induced doping of ordered mesoporous TiO₂ thin films for visible light active photocatalysis, *Microporous Mesoporous Mater.* 220 (2016) 120–128. <https://doi.org/10.1016/j.micromeso.2015.08.030>.
- [25] A. Karpinski, S. Berson, H. Terrisse, M. Mancini-Le Granvalet, S. Guillerez, L. Brohan, M. Richard-Plouet, Anatase colloidal solutions suitable for inkjet printing: Enhancing lifetime of hybrid organic solar cells, *Sol. Energy Mater. Sol. Cells*. 116 (2013) 27–33. <https://doi.org/10.1016/j.solmat.2013.04.006>.
- [26] N. Sahu, B. Parija, S. Panigrahi, Fundamental understanding and modeling of spin coating process: A review, *Indian J. Phys.* 83 (2009) 493–502. <https://doi.org/10.1007/s12648-009-0009-z>.
- [27] M. Banik, R. Mukherjee, Fabrication of Ordered 2D Colloidal Crystals on Flat and Patterned Substrates by Spin Coating, *ACS Omega*. 3 (2018) 13422–13432. <https://doi.org/10.1021/acsomega.8b02002>.
- [28] F. Nicolazo, A. Goulet, A. Granier, C. Vallee, G. Turban, B. Grolleau, Study of oxygen/TEOS plasmas and thin SiO_x films obtained in an helicon diffusion reactor, *Surf. Coat. Technol.* 98 (1998) 1578–1583.

- [29] A. Granier, G. Borvon, A. Bousquet, A. Goulet, C. Leteinturier, A. van der Lee, Mechanisms Involved in the Conversion of ppHMDSO Films into SiO₂-Like by Oxygen Plasma Treatment, *Plasma Process. Polym.* 3 (2006) 365–373. <https://doi.org/10.1002/ppap.200600022>.
- [30] A. Granier, F. Nicolazo, C. Vallée, A. Goulet, G. Turban, B. Grolleau, Diagnostics in helicon plasmas for deposition, *Plasma Sources Sci. Technol.* 6 (1997) 147–156. <https://doi.org/10.1088/0963-0252/6/2/008>.
- [31] D. Saha, R.S. Ajimsha, K. Rajiv, C. Mukherjee, M. Gupta, P. Misra, L.M. Kukreja, Spectroscopic ellipsometry characterization of amorphous and crystalline TiO₂ thin films grown by atomic layer deposition at different temperatures, *Appl. Surf. Sci.* 315 (2014) 116–123. <https://doi.org/10.1016/j.apsusc.2014.07.098>.
- [32] D. Li, M. Carette, A. Granier, J.P. Landesman, A. Goulet, In situ spectroscopic ellipsometry study of TiO₂ films deposited by plasma enhanced chemical vapour deposition, *Appl. Surf. Sci.* 283 (2013) 234–239. <https://doi.org/10.1016/j.apsusc.2013.06.091>.
- [33] B. Enright, D. Fitzmaurice, Spectroscopic Determination of Electron and Hole Effective Masses in a Nanocrystalline Semiconductor Film, *J. Phys. Chem.* 100 (1996) 1027–1035. <https://doi.org/10.1021/jp951142w>.
- [34] R. Vijayalakshmi, V. Rajendran, Synthesis and characterization of nano-TiO₂ via different methods, *Arch. Appl. Sci. Res.* 4 (2012) 1183–1190.
- [35] H.G. Tompkins, ed., *Handbook of ellipsometry*, Repr, Andrew [u.a.], Norwich, NY, 2010.
- [36] S.O. Kasap, *Principles of electronic materials and devices*, McGraw-Hill, Boston, 2006.

- [37] J. Profili, O. Levasseur, J.-B. Blaisot, A. Koronai, L. Stafford, N. Gherardi, Nebulization of Nanocolloidal Suspensions for the Growth of Nanocomposite Coatings in Dielectric Barrier Discharges: Nebulization of Nanocolloidal Suspensions..., *Plasma Process. Polym.* 13 (2016) 981–989. <https://doi.org/10.1002/ppap.201500223>.
- [38] A.B.D. Nandiyanto, K. Okuyama, Progress in developing spray-drying methods for the production of controlled morphology particles: From the nanometer to submicrometer size ranges, *Adv. Powder Technol.* 22 (2011) 1–19. <https://doi.org/10.1016/j.appt.2010.09.011>.
- [39] W.F. Zhang, Y.L. He, M.S. Zhang, Z. Yin, Q. Chen, Raman scattering study on anatase TiO₂ nanocrystals, *J. Phys. Appl. Phys.* 33 (2000) 912–916. <https://doi.org/10.1088/0022-3727/33/8/305>.
- [40] T. Ohsaka, F. Izumi, Y. Fujiki, Raman spectrum of anatase, TiO₂, *J. Raman Spectrosc.* 7 (1978) 321–324. <https://doi.org/10.1002/jrs.1250070606>.
- [41] W. Ma, Z. Lu, M. Zhang, Investigation of structural transformations in nanophase titanium dioxide by Raman spectroscopy, *Appl. Phys. Mater. Sci. Process.* 66 (1998) 621–627. <https://doi.org/10.1007/s003390050723>.
- [42] C. Pighini, D. Aymes, N. Millot, L. Saviot*, Low-frequency Raman characterization of size-controlled anatase TiO₂ nanopowders prepared by continuous hydrothermal syntheses, *J. Nanoparticle Res.* 9 (2007) 309–315. <https://doi.org/10.1007/s11051-005-9061-6>.
- [43] A.G. Rolo, M.I. Vasilevskiy, Raman spectroscopy of optical phonons confined in semiconductor quantum dots and nanocrystals, *J. Raman Spectrosc.* 38 (2007) 618–633. <https://doi.org/10.1002/jrs.1746>.

- [44] Y. Gao, X. Zhao, P. Yin, F. Gao, Size-Dependent Raman Shifts for nanocrystals, *Sci. Rep.* 6 (2016).
<https://doi.org/10.1038/srep20539>.
- [45] J. Profili, O. Levasseur, N. Naudé, C. Chaneac, L. Stafford, N. Gherardi, Influence of the voltage waveform during nanocomposite layer deposition by aerosol-assisted atmospheric pressure Townsend discharge, *J. Appl. Phys.* 120 (2016) 053302. <https://doi.org/10.1063/1.4959994>.
- [46] D. Li, S. Elisabeth, A. Granier, M. Carette, A. Goulet, J.-P. Landesman, Structural and Optical Properties of PECVD TiO₂-SiO₂ Mixed Oxide Films for Optical Applications: Structural and Optical Properties of PECVD TiO₂-SiO₂ ..., *Plasma Process. Polym.* 13 (2016) 918–928.
<https://doi.org/10.1002/ppap.201600012>.
- [47] J.F. Moulder, W.F. Stickle, P.E. Sobol, K.D. Bomben, J. Chastain, R.C. King Jr., Physical Electronics, Incorporation, eds., *Handbook of X-ray photoelectron spectroscopy: a reference book of standard spectra for identification and interpretation of XPS data*, Physical Electronics, Eden Prairie, Minn., 1995.
- [48] G.H.P.M. Swinkels, H. Kersten, H. Deutsch, G.M.W. Kroesen, Microcalorimetry of dust particles in a radio-frequency plasma, *J. Appl. Phys.* 88 (2000) 1747–1755.
<https://doi.org/10.1063/1.1302993>.
- [49] N.J. Kramer, R.J. Anthony, M. Mamunuru, E.S. Aydil, U.R. Kortshagen, Plasma-induced crystallization of silicon nanoparticles, *J. Phys. Appl. Phys.* 47 (2014) 075202.
<https://doi.org/10.1088/0022-3727/47/7/075202>.

- [50] A.-L. Thomann, A. Caillard, M. Raza, M. El Mokh, P.A. Cormier, S. Konstantinidis, Energy flux measurements during magnetron sputter deposition processes, *Surf. Coat. Technol.* 377 (2019) 124887. <https://doi.org/10.1016/j.surfcoat.2019.08.016>.
- [51] A. Granier, S. Jacq, D. Li, M. Carette, A. Goulet, Investigation of plasma surface interactions in pulsed O₂/TTIP low pressure ICP plasma by time resolved optical emission spectroscopy, in: *ESCAMPIG XXI*, Viana do Castelo, Portugal, 2010: p. 2.
- [52] R. Piejak, V. Godyak, B. Alexandrovich, N. Tishchenko, Surface temperature and thermal balance of probes immersed in high density plasma, *Plasma Sources Sci. Technol.* 7 (1998) 590–598. <https://doi.org/10.1088/0963-0252/7/4/016>.
- [53] H. Kersten, H. Deutsch, H. Steffen, G.M.W. Kroesen, R. Hippler, The energy balance at substrate surfaces during plasma processing, *Vacuum.* 63 (2001) 385–431. [https://doi.org/10.1016/S0042-207X\(01\)00350-5](https://doi.org/10.1016/S0042-207X(01)00350-5).
- [54] Y. Qi, B. Xiang, J. Zhang, Effect of titanium dioxide (TiO₂) with different crystal forms and surface modifications on cooling property and surface wettability of cool roofing materials, *Sol. Energy Mater. Sol. Cells.* 172 (2017) 34–43. <https://doi.org/10.1016/j.solmat.2017.07.017>.
- [55] V.L. Popov, M. Heß, E. Willert, Normal Contact Without Adhesion, in: *Handb. Contact Mech.*, Springer Berlin Heidelberg, Berlin, Heidelberg, 2019: pp. 5–66. https://doi.org/10.1007/978-3-662-58709-6_2.
- [56] S. Prasanna, A. Michau, K. Hassouni, S. Longo, Effect of charge fluctuation on nanoparticle heating in dusty plasma, *Plasma Sources Sci. Technol.* 28 (2019) 03LT03. <https://doi.org/10.1088/1361-6595/ab094d>.

- [57] A. Lamberti, A. Chiodoni, N. Shahzad, S. Bianco, M. Quaglio, C.F. Pirri, Ultrafast Room-Temperature Crystallization of TiO₂ Nanotubes Exploiting Water-Vapor Treatment, *Sci. Rep.* 5 (2015). <https://doi.org/10.1038/srep07808>.
- [58] L. Yang, M. Zhang, S. Shi, J. Lv, X. Song, G. He, Z. Sun, Effect of annealing temperature on wettability of TiO₂ nanotube array films, *Nanoscale Res. Lett.* 9 (2014) 621. <https://doi.org/10.1186/1556-276X-9-621>.
- [59] F. Hilario, V. Roche, R.P. Nogueira, A.M.J. Junior, Influence of morphology and crystalline structure of TiO₂ nanotubes on their electrochemical properties and apatite-forming ability, *Electrochimica Acta.* 245 (2017) 337–349. <https://doi.org/10.1016/j.electacta.2017.05.160>.
- [60] S. Kundu, V. Polshettiwar, Hydrothermal Crystallization of Nano-Titanium Dioxide for Enhanced Photocatalytic Hydrogen Generation, *ChemPhotoChem.* 2 (2018) 796–800. <https://doi.org/10.1002/cptc.201800101>.
- [61] H. Ohsaki, Y. Shibayama, N. Yoshida, T. Watanabe, S. Kanemaru, Room-temperature crystallization of amorphous films by RF plasma treatment, *Thin Solid Films.* 517 (2009) 3092–3095. <https://doi.org/10.1016/j.tsf.2008.11.086>.